Journal of Physics and Chemistry of Solids 136 (2020) 109156

Contents lists available at ScienceDirect

Journal of Physics and Chemistry of Solids

journal homepage: www.elsevier.com/locate/jpcs

Unraveling the stacking effect and stability in nanocrystalline antimony through DFT

Showkat Hassan Mir[a], Vivek Kumar Yadav[b], Jayant Kumar Singh[b,*]

[a] Department of Chemistry, IIT Kanpur, Kanpur, 208016, India
[b] Department of Chemical Engineering, IIT Kanpur, Kanpur, 208016, India

A B S T R A C T

Two-dimensional nanocrystals with semiconducting electronic properties are emerging as promising materials for electronic devices. Here, we present the density functional theory calculations of structural stability, Raman spectra and electronic properties of monolayer, bilayer (AA and AB stacking) and trilayer (AAA and ABC stacking) antimony (Sb). The cohesive energy and phonon band dispersion results revealed that free-standing Sb systems are stable materials. Calculated Raman spectra showed distinct active modes, thus facilitating the characterisation of multilayered structures in different stacking arrangements. It was found that high-frequency in-plane (E_g) and out-of-plane (A_{1g}) modes can shift as much as 16 cm^{-1} and 28 cm^{-1} as the layer number increases from monolayer to trilayer. Band structure calculations showed that monolayer and bilayer (AA stacked) Sb are semiconductors with band gap values 1.26 eV and 0.55 eV, respectively, whereas bilayer (AB) and trilayer Sb displayed metallic character. Spin-orbit coupling interaction was also incorporated in band structure calculations and was found to reduce the band gap of monolayer Sb to 1.0 eV while it does not effect on the band gap values of other systems. Moreover, it was seen that nanocrystalline Sb exhibit isotropic mechanical properties. The carrier mobility calculations showed that electron/hole mobility increases by 5/32 times from monolayer to trilayer, respectively.

1. Introduction

Two-dimensional (2D) crystals have emerged as an exciting class of materials, which shows unique and extraordinary properties and have promising applications. Typically, graphene allows electrons to flow freely across its surfaces, which results in huge electron mobility that enables its superior performance in transistors and as an excellent electrochemical electrode [1]. However, the electronic structure of graphene show a zero band gap [2], which severely reduces its ability to switch current on and off in transistors. Even by surface functionalization and application of external electric or strain fields, very small band gaps can be achieved [3,4]. The other elemental monolayers of group IV, namely, silicene and germanene which are analogous of graphene also exhibit a zero band gap [5,6]. Two-dimensional boron sheets are also found to show metallic nature [7,8]. Considering the application of 2D nanocrystalline structures in transistors, the identification of new semiconducting materials with finite band gaps is of utmost importance. The search for contenders of graphene has led to the prediction or synthesis of new nanocrystals and their van der Waals heterostructures. For instance, graphene analogous of group IV elements [9], group II-VI, III-V and IV-IV compounds [10], which are similar to h-BN, and other 2D nanocrystals such as graphynes [11] and borocarbonitride (BCN) [12–14] have been actively studied. Moreover, transition metal dichalcogenides were also investigated and are found to show superior optoelectronic applications in several areas in comparison to graphene [15–17]. Recently, the elemental monolayers of group V have emerged as novel 2D materials with semiconducting electronic properties [5,9,18–20], thereby, offering prospects for nanoelectronic application. For instance, the monolayered black phosphorene (BP) were found to possess a direct band gap and high carrier mobility [20], making it attractive for electronic applications. However, due to severe instability of BP in air, its practical applications are very challenging [21,22]. It has been reported that thin samples of black phosphorus with 10 nm thickness may degrade in days while few-layer or monolayer BP nanocrystals may degrade within hours. Another issue that hinders the practical application of BP is the difficulty in synthesizing of samples [23]. Though, nanosheets of BP can be exfoliated using scotch tape or by liquid exfoliation method from bulk black phosphorus, however, the bulk black phosphorus itself is produced from red phosphorus under high pressure or temperature [23]. Thus, making the direct synthesis of atomically thin BP greatly challengeable. In contrast to BP, another elemental 2D materials composed of group V, namely, nanocrystalline Sb, was recently predicted to have superior stability, as well as extraordinary properties from theoretical calculations [5,9,18,23–25]. Further, Zhang et al. [5] predicted that among several possible allotropes, the rhombohedral phase, usually viewed as ABC stacking of monolayer Sb exhibit the highest stability. They also predicted that the band structures of Sb would transfer from semimetal

* Corresponding author.
E-mail address: jayantks@iitk.ac.in (J.K. Singh).

https://doi.org/10.1016/j.jpcs.2019.109156
Received 14 June 2019; Received in revised form 7 August 2019; Accepted 18 August 2019
Available online 19 August 2019
0022-3697/

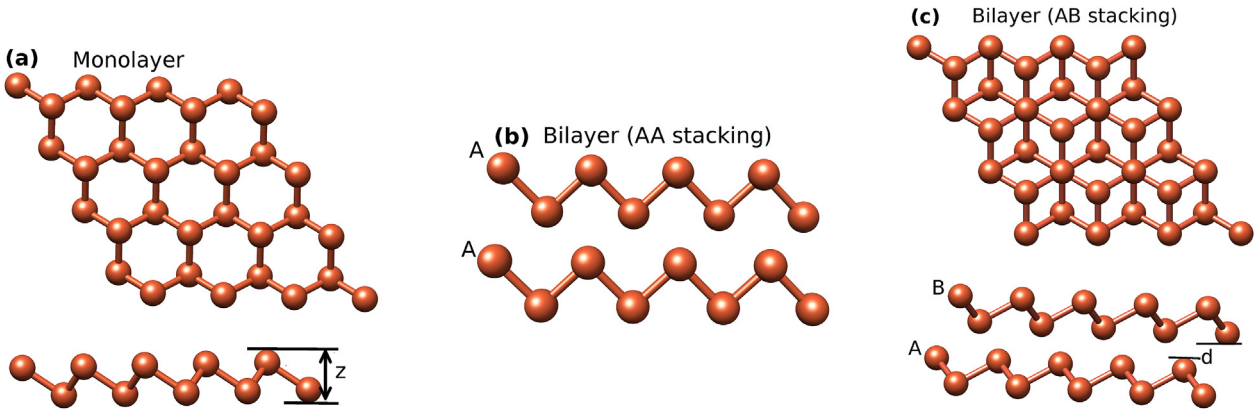

Fig. 1. Top and side view of the crystal structures of (a) monolayer, (b,c) bilayer antimony in AA and AB stacking.

in the bulk form into semiconductor when thinned to one atomic layer. According to theoretical calculations, nanocrystalline Sb presents superior thermal conductivity [18], strain induced band transition [24] and promising spintronic properties [25]. Using molecular beam epitaxy, Lei et al. has reported the synthesis of ML Sb on Sb_2Te_3 and Bi_2Te_3 [26]. Also, flakes of nanocrystalline Sb were synthesized through mechanical exfoliation [27]. Moreover, Tsai et al. claimed the synthesis of multilayered Sb nanoribbons with thickness about 20 nm and observed the orange light emission, which they attributed to quantum confinement effect and turbostratic stacking order [28]. Due to the tremendous difference between various possible allotropes of nanocrystalline Sb, identification of the exact atomic structure of synthesized Sb samples is also very important. In this case, the experimental synthesis of high-quality and nanocrystalline Sb together with systematic atomic structure characterizations is urgent for the emerging research hotspots of group V elemental 2D materials. In this work, we focus on monolayer (ML), bilayer (BL) with AA and AB stacking and trilayer (TL) with AAA and ABC stacking Sb using density functional theory (DFT). The stability of nanocrystalline Sb was examined by phonon dispersion and cohesive energy calculations. Raman spectra was calculated, which can be helpful to characterize the thickness of Sb and their different stacking arrangements. The band structures of various nanocrystalline Sb systems were calculated with spin-orbit coupling (SOC). Moreover, the carrier mobility is predicted using deformation potential theory[30?]

2. Methodology

First principles calculations were performed to study the ground state properties of ML, BL and TL Sb using QUANTUM ESPRESSO [31] code within the framework DFT. The electron-ion interaction was described by Perdew-Burke-Ernzerhof [32] functional with generalized gradient approximation (GGA) [33]. To obtain the minimum energy structure, the Kohn-Sham wave-functions were expanded by a plane wave basis set with a kinetic energy cut-off of 50 Ry for wavefunction and 500 Ry for charge density. Brillouin zone (BZ) integration was done using a uniform Γ-centered Monkhorst-Pack [34] k-point grid of $25 \times 25 \times 1$ for geometry optimization and $35 \times 35 \times 1$ for self-consistent field calculations. The atomic positions and cell parameters were fully relaxed until an energy convergence of 10^{-8} eV is achieved and force on each atom was smaller than 0.01 eV/Å. van der Waals interactions were included using DFT-D3 dispersion corrections [35]. A vacuum of 20 Å was used in the z-direction to eliminate the interslab interactions. The spin-orbit coupling (SOC) was also included for band structure calculations.

The density functional perturbation theory (DFPT) was used to calculate the phonon band structure and Raman spectra in the linear response approach [36,37]. For phonon bands dispersion, we used q-point grid of $6 \times 6 \times 1$ for ML and $4 \times 4 \times 1$ for BL and TL. The standard norm-conserving local density functional (LDA) pseudopotentials [38] were employed for Raman spectra calculations.

The carrier mobility of nanocrystalline Sb was also predicted in the deformation potential (DP) theory approximation using the formula [29,30],

$$\mu_{2D} = \frac{e\hbar^3 C^{2D}}{k_B T m^{*2} (E^i)^2} \quad (1)$$

where m* denotes the effective mass of charge carriers, E^i represents the DP constant of the conduction band minimum (CBM) for electrons or valence band maximum (VBM) for holes along the transport direction and is defined as, $E^i = \Delta E_i/\varepsilon$. Here ΔE_i is the energy change of an ith band under cell compression or dilatation, ε is the applied strain, which is defined as $\varepsilon = \Delta l/l_0$, where l_0 is the equilibrium lattice constant in the transport direction and Δl_0 is the deformation of l_o. The effective mass is calculated by parabolic fitting of the E versus k curve ($m_*^{-1} = \frac{1}{\hbar^2}\frac{\partial^2 E}{\partial k^2}$) for holes and electrons in the vicinity of VBM and CBM, respectively. The elastic modulus C_{2D} along x- and y-direction is calculated as a second derivative of energy with respect to the applied uniaxial strain per unit area as, $C^{2D} = \frac{1}{S_o}\frac{d^2E}{d\varepsilon^2}$, where E denotes the total energy of deformed system and S_0 is the area of the system at equilibrium. The strain was varied from −1% to 1% in steps of 0.25. All these parameters were calculated using PBE functional. The temperature used for mobility calculation is 300 K.

3. Results and discussion

3.1. Structural properties and Raman spectra

The optimized stable crystal structures of ML, BL, and TL Sb are shown in Fig. 1 (optimized structures of TL Sb are shown in Fig. S1.) In Table 1, the lattice parameters, bond lengths (R), thickness (z), smallest interplanar distance (d) and cohesive energy of Sb nanocrystals are presented. These nanocrystals have a hexagonal symmetry with buckled structure. The predicted lattice parameter of ML Sb is 4.11 Å. The calculated bond length between neighboring Sb atoms is 2.88 Å and the bond angle is 90.91°. Thickness of the ML Sb calculated is 1.64 Å. These results are in consistent with previous theoretical calculations [18]. Furthermore, each Sb atom (with five valence electrons) is bonded to three adjacent atoms in the same layer, which endows them with octet stability. The buckled honeycomb structure, similar to those of silicene and germanene, also helps stabilize the layered structure [6]. It is observed that bond length increases minutely (~1pm) for BL and TL Sb in AA and AAA stacked arrangement relative to ML, while the bond length increases by 0.13 Å and 0.17 Å for BL and TL Sb in AB and ABC stacked form. It is interesting to note that we did not observe any change in the thickness of BL (TL) Sb in AA (AAA) stacking relative to ML. However, it is seen that for BL and TL Sb in AB and ABC stacking, the layer

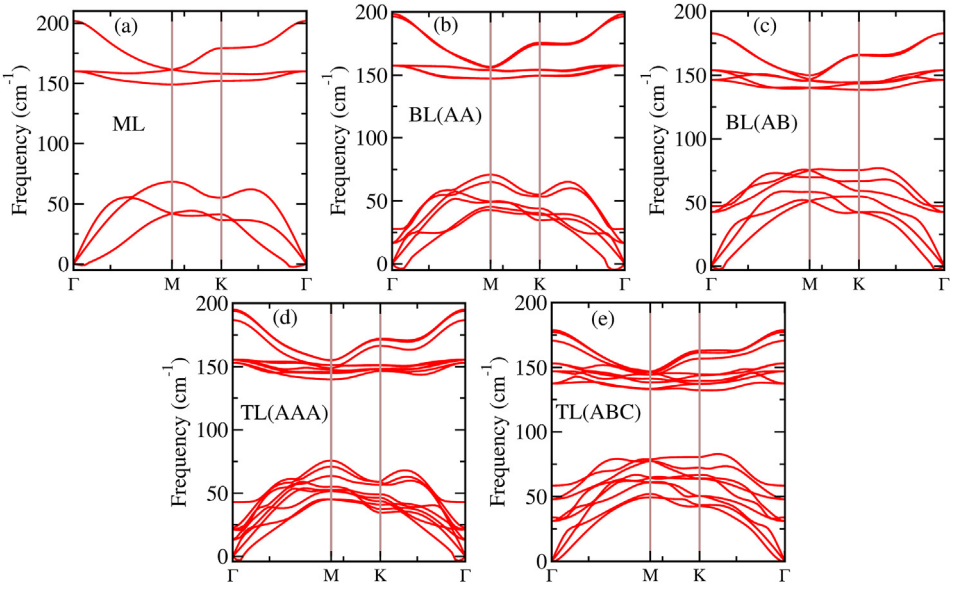

Fig. 2. Phonon band structure of (a) monolayer, (b,c) bilayer AA and AB stacked and (d,e) trilayer AAA abd ABC stacked antimony showing the lattice dynamic stability of all structures.

thickness decreases by 0.07 Å and 0.09 Årelative to the ML. Also, the interlayer spacing in BL (TL) Sb in AA (AAA) stacking increases by 0.76 Å(0.94 Å) in comparison to the bulk Sb. On the other hand, it can be seen that for BL (TL) Sb in AB (ABC) stacking, increase in interlayer spacing is only by 0.12 Å(0.09 Å) relative to bulk interlayer distance. These results indicate that AB and ABC stacking is more stable compared to AA or AAA arrangement. The calculated ground state energies also revealed that AB (ABC) arrangements are more stable by 7.83 meV (19.35 meV) than AA (AAA) Sb. This also indicates that AB (ABC) stacking have a strong interlayer interaction compared to AA (AAA) stacking. It is important to note that bulk Sb also crystallize in ABC stacking [9](Fig. S2). The lattice parameter **a(c)** calculated for bulk Sb is 4.36 (11.25) Å, which agrees well with previous experimental [39] and theoretical [9,18] results.

Stability and experimental feasibility are important properties of a material for its applications. In order to examine the stability of ML and few-layer Sb, we calculated the phonon dispersion as shown in Fig. 2. It is well known that phonon dispersion showing soft modes (negative frequency) indicates the instability of a lattice. From phonon dispersion (Fig. 2), it is apparent that no vibrating mode has negative frequency in the computed dispersion spectra of ML, BL and TL Sb, which illustrates their dynamic stability as free standing layers. A significant dispersion 60 cm^{-1} is found in the longitudinal modes and a frequency gap of about 90 cm^{-1} between the acoustic and optical modes for ML Sb. The highest phonon frequency of optical modes at Γ-point found for ML Sb is 200 cm^{-1}. This phonon frequency decreases for BL (AB) and TL (ABC) to 170 cm^{-1} and 155 cm^{-1} whereas, only a small decrease (5 cm^{-1}) is seen for BL (AA) and TL (AAA) nanocrystals. The phonon dispersion shows similar behavior for three structures. A small negative frequency ($<5cm^{-1}$) seen in the phonon dispersion at Γ-point occurs due to numerical errors.

The stability of nanocrystalline Sb were further investigated by calculating cohesive energy at PBE level with and without spin orbit coupling. Cohesive energy (E_{coh}) of different layered Sb was calculated using equation $E_{coh} = [E_{tot} - n_i E_{Sb}]/n \quad (i = 2, 4, 6)$, where, E_{tot} denotes the total energy of nanocrystal structure, E_{Sb} represents the gas phase atomic energy of Sb and n_i represents the total number of atoms in the sheet. The calculated cohesive energies are shown in Table 1. It is found that the cohesive decreases when SOC is incorporated in the calculations. However, both approaches indicate a similar trend in the thermodynamic stability of various nanocrystals. Moreover, it is

Table 1
The calculated lattice parameters, bond lengths, thickness, smallest interlayer distances and cohesive energies per atom of ML, BL and TL antimony. Bracketted values represent the lattice vector **c** for bulk antimony.

	structure	a/Å	R/Å	z/Å	d/Å	$E_{coh}(eV)$	$E_{coh}^{SOC}(eV)$
Present	ML	4.11	2.88	1.64	–	−3.98	−3.49
Others [18]	ML	4.12	2.89	–	–	−4.03	–
Present	BL (AA)	4.13	2.89	1.64	3.17	−4.04	−3.54
Present	BL (AB)	4.24	2.91	1.57	2.35	−4.07	−3.57
Present	TL (AAA)	4.12	2.89	1.64	2.99	−4.07	−3.57
Present	TL (ABC)	4.28	2.91	1.56	2.32	−4.11	−3.61
Present	Bulk	4.36 (11.25)	2.94	1.52	2.23	−4.21	−3.76
Expt [39].	Bulk	4.31 (11.27)	2.91	–	–	–	–
Others [18]	Bulk	4.31 (11.27)	–	–	–	–	–

apparent from Table 1 that as the number of layers increases the cohesive energy also increases, which shows that multilayer Sb structures are more stable compared to monolayered antimony. As shown in Table, BL (AA) and TL (AAA) antimony nanocrystals are more stable than ML by 90 meV (70 meV) and 130 meV (90 meV), respectively. The binding energy per atom of bilayer and trilayer Sb was also calculated using the equation $E_b = (E_{tot} - mE_{ML})/N$, where E_{tot} is the energy of BL/TL Sb, E_{ML} represents the energy of monolayer sheet, m is the number of layers and N is the total number of atoms in BL/TL Sb. The calculated binding energy of AA and AB stacked Sb was −57.69 eV and −84.35 eV, respectively. Similarly, calculated binding energy of TL Sb was −81.11 meV and −124.98 meV for AAA and ABC stacked Sb. The results show that ABC stacked Sb is energetically more stable than AAA type. Experimentally, the binding energy of trilayer ABA and ABC stacked graphene was found to be −105 meV and −117 meV [40]. These results show that TL Sb show a similar trend as exhibited by TL graphene.

Considering that Raman measurements are generally employed to characterize 2D materials [41] (e.g. graphene), we also calculated the Raman spectra of ML, BL and TL Sb at LDA + DFT level. As LDA pseudopotentials always underestimates the lattice constants, therefore, all structures were fully re-optimized at LDA level for Raman spectra calculation. Lattice constant calculated using LDA are shown in Table S1. The Raman spectra of ML and BL Sb are shown in Fig. 3. The Raman peak frequencies of different modes were fitted by Gaussian profile with 2 cm^{-1} line-width using Magicplot software [42]. To evaluate the

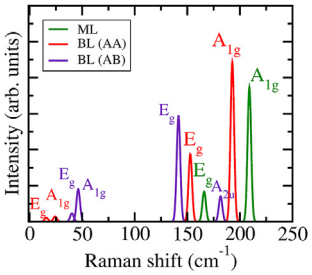

Fig. 3. The calculated Raman spectra of ML and BL antimony. A convolution of the computed DFT spectra with a Gaussian profile with 2 cm^{-1} line-width was performed for better visualization using Magicplot software [42].

reliability of the present methodology, we first computed the Raman spectrum of bulk Sb (Fig. S3). Two Raman peaks, E_g at 99 cm^{-1} and A_{1g} at 146.4 cm^{-1} were seen that are in agreement with experimental results of E_g (110 cm^{-1}) and A_{1g} (149.8 cm^{-1}) [39]. This gives confidence in our calculated results for the Raman spectra of free standing Sb. Two active Raman modes E_g at 166 cm^{-1} and A_{1g} at 209 cm^{-1} were seen for ML Sb, which agrees well with the previous theoretical results [18]. The peak frequencies of both modes were found to show blue shift (i.e. move to higher frequency region) with respect to the bulk Sb. A blue-shift trend of Raman peak frequencies by decreasing thickness have been observed in the Raman studies of other 2D materials [43,44]. E_g is an in-plane vibrating mode where the two atoms in the unit cell vibrate in opposite direction. A_{1g} is the out-of-plane (flexural) vibrating mode (Fig. S4). This Raman spectra is the characteristic of ML Sb. In BL (AA stacking) Sb, besides, E_g and A_{1g} modes, two additional peaks at lower frequencies were also observed as shown in Fig. 3. Considering the E_g (153 cm^{-1}) and A_{1g} (193 cm^{-1}) modes, it was seen that their peak frequencies show red-shift compared to the ML Sb. A shit of 13 cm^{-1} and 16 cm^{-1} were observed for E_g and A_{1g} modes, respectively. The peak frequency of other two modes calculated were 15 cm^{-1} for E_g and 24 cm^{-1} for A_g. The A_{1g} (193 cm^{-1}) was the dominating Raman peak for AA stacked BL Sb for which atoms belonging to the same sublayer vibrate out-of-plane in the same direction. In A_g (24 cm^{-1}), the atoms belonging to the same sublayer vibrate along the same direction and the two sublayers vibrate opposite to each other. The E_g (152 cm^{-1}) and E_g (15 cm^{-1}) modes are in-plane vibrations, whereas atoms in the sublayer vibrate along opposite direction in the former and along the same direction in later. In AB stacked BL, the Raman modes observed are E_g at 41 cm^{-1} and 142 cm^{-1}, and A_{1g} at 45 cm^{-1} and A_{2u} at 181 cm^{-1} . The atoms vibrate in the same fashion as in AA stacked BL for E_g and A_{1g}, while in A_{2u} mode, the atoms in two sublayers vibrate in opposite direction. Here, also a red shift of 24 cm^{-1} (25 cm^{-1}) was seen for high frequency E_g (A_{2u}) mode relative to the ML Sb. Besides, AB stacked BL also realizes a red shift with respect to the AA stacked BL Sb. Furthermore, AAA stacked TL, six vibrating modes were found to be Raman active. These modes are E_g with peak frequencies 13 cm^{-1} and 152 cm^{-1}, E_u at 152 cm^{-1}, A_{1g} at 25 cm^{-1} and 188 cm^{-1} and A_{2u} at 194 cm^{-1}, respectively. While for ABC stacked TL, seven modes were found to be Raman active. The peak frequencies of the various modes were 36 cm^{-1}, 141 cm^{-1} and 157 for E_g mode, 40 cm^{-1} and 180 cm^{-1} for A_{1g} mode, 68 cm^{-1} and 184 cm^{-1} for A_{2u} modes, respectively. The atomic vibrations of Raman modes for BL and TL Sb are plotted in Fig. S5. Thus, from the analysis of Raman modes, it is seen that there is an obvious shift in the peak frequencies both with the layer numbers and stacking arrangement, which will be helpful in the characterisation of nanocrystalline Sb.

3.2. Electronic structure

The calculated band structure of ML, BL (AA, AB stacked) and TL (AAA, ABC stacked) Sb at PBE level including SOC are shown in Fig. 4. From the band structure, it is seen that ML Sb exhibit an indirect bandgap with valence band maximum (VBM) located at Γ-point whereas the conduction band minimum (CBM) occurs between Γ and M symmetric points of Brillouin zone (BZ). The band gap calculated for ML Sb using PBE functional was 1.26 eV which reduces to 1.0 eV when SOC is included. It is clear from Fig. 4(a) that when SOC is included, both CBM and VBM shifts towards Fermi energy, which causes a reduction in the band gap. The calculated band gap and its reduction with SOC is consistent with the results of Lee et al. [25]. They also realized a reduction in band gap of two-dimensional bismuth with SOC. In fact, it is observed that SOC causes the shift of CB throughout the BZ whereas VB exhibit a shift only at Γ-point. It is also apparent from Fig. 4(a) that SOC removes the degeneracy of bands at symmetric points K and M as well as along the path K to M. For BL Sb in AB stacking arrangement, band gap is 0 eV. However, it is important to note that AA stacked BL shows a band gap of 0.55 eV, which makes AA stacked bilayer an interesting candidate material compared to the AB stacked Sb that shows a 0 eV band gap. Moreover, it is apparent from the band structure that both conduction and valence band shifts towards Fermi level, which decreases the band gap of BL Sb. Nevertheless, the AA stacked BL maintain a band gap, while the band edges AB of stacked BL touch the Fermi level. From the band structure, it is also revealed that SOC has not a significant effect on the band gaps of the BL structures, though it removes the degeneracy at K and M symmetry points. It is also noteworthy to see that TL Sb (AAA stacking) show semi-metallic character, while ABC stacked TL exhibit a trivial metallic behavior. Again, no significant role of SOC has been observed in TL Sb. Further, it can be noticed from the band dispersion that conduction and valence band edges are different for multilayered Sb. The AA and AAA stacked Sb show band dispersion similar to ML Sb whereas AB and ABC stacked structures exhibit completely different dispersion of bands. Carrier mobility is a dominant feature to assess the electrical performance of materials. The carrier mobility and other related parameters obtained for nanocrystalline Sb are shown in Table 2. The effective mass for electron and hole shown in the Table were calculated at CBM and VBM, respectively. The effective mass of electron in monolayer and hole in bilayer Sb is found to be slightly larger than free electron mass. For all other cases, the effective mass is smaller than mass of free electron. As Sb nanocrystals exhibit similar atomic arrangement along x-and y-direction, therefore, it is expected that mechanical properties and carrier mobility should be isotropic. From Table 2, it is apparent that elastic constants of various Sb nanocrystals display isotropic nature. Carrier mobility is also found to be isotropic. The small differences may be due to numerical errors. It is seen that electron mobility is higher than hole mobility in ML Sb. The mobility is found to be ~3 (~2) times larger along x(y) direction. In a previous theoretical calculation, the electron/hole mobility values ($21/66 cm^2V^{-1}s^{-1}$) of ML arsenic were found to be of the same order [45]. The electron/hole mobility of BL and TL were found to be larger than ML Sb. It is found that the carrier mobility increases as the number of layers increases. However, for multilayer Sb, the hole mobility was found to be larger than the electron mobility. The carrier mobility in BL and TL Sb is higher or comparable to that of graphene [46] (~ $170 cm^2V^{-1}s^{-1}$) and MoS_2 [47] (~ $200 cm^2V^{-1}s^{-1}$).

4. Conclusions

DFT calculations were performed to investigate the structural properties, Raman spectra and electronic band structure of nanocrystalline Sb. The phonon band dispersion confirmed that free-standing ML, BL and TL Sb are dynamically stable structures. Cohesive energy results also showed their thermodynamic stability. From the calculated cohesive energy results, it was found that stability increases with increase in layer number. Also, it was found that AB stacked BL Sb is more stable than AA stacked BL. Similar conclusions were drawn for AAA and ABC stacked TL Sb systems. The Raman spectra showed two active modes for ML Sb at 209 cm^{-1} and 166 cm^{-1}. In the case of BL Sb with

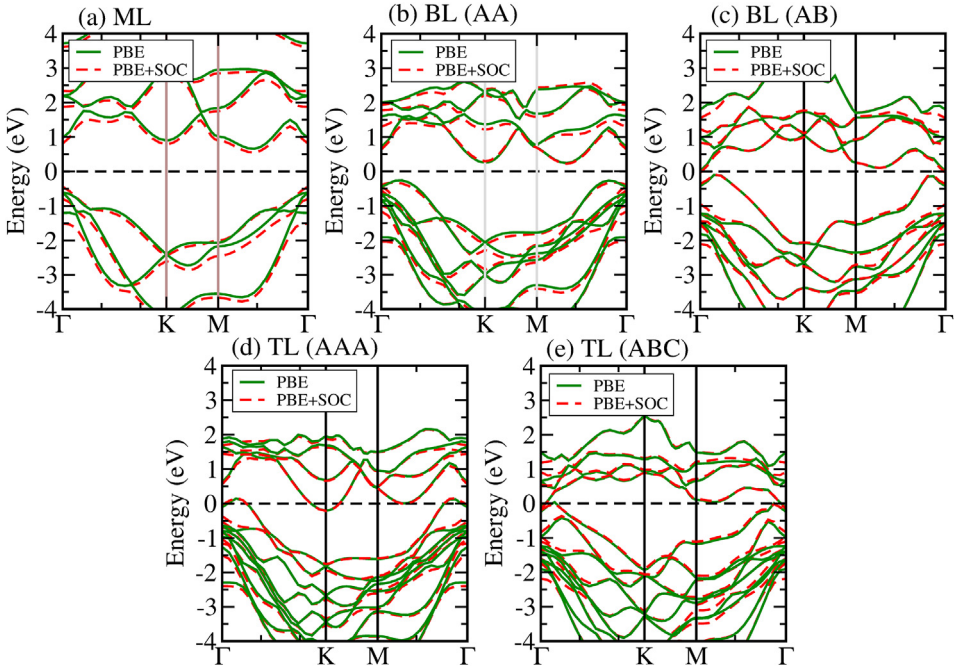

Fig. 4. The electronic band structure of (a) monolayer (b,c) bilayer AA and AB stacked and (d,e) trilayer AAA and ABC stacked antimony calculated with and without spin-orbit coupling. Fermi level is set at 0 eV.

Table 2
Carrier, 'e' and 'h' denote electron and hole respectively.N_L represents the number of layers, m* is the effective mass of carriers. E_x, E_y C_x^{2D} and C_y^{2D} represents the deformation potential and elastic constants for directions x and y, respectively. μ_x and μ_y denote the mobilities ($cmcm^2V^{-1}s^{-1}$).

Carrier	N_L	m_*/m_o	E_x	E_y	C_x^{2D}	C_y^{2D}	μ_x	μ_y
e	ML	1.03	3.76	4.32	32.55	32.69	44.78	34.16
	BL	0.86	5.74	5.47	59.26	57.79	52.13	55.97
	TL	0.81	3.94	3.76	75.05	74.32	157.1	171.41
h	ML	0.93	7.39	7.31	32.55	32.69	14.64	15.04
	BL	1.09	3.15	2.51	59.26	57.79	107.41	165.44
	TL	0.47	3.82	3.82	75.05	74.32	492.96	488.38

m_o is the rest mass of electron.

AA and AB stacking arrangement, four Raman modes were observed, which were found to show a red shift with respect to the ML Sb. Similar trend was also seen for TL Sb nanocrystals and all modes were found to have distinct peak frequencies. It is expected that present theoretical calculations and analysis of Raman spectra will provide a way to the unambiguous identification of layer numbers for nanocrystalline Sb in experiments with different stacking arrangement. From electronic band structure, ML and BL (AA stacked) Sb were found to show indirect band gap of 1.26 eV and 0.55 eV, whereas the other systems were found to display metallic character. The SOC interaction were seen to reduce the band gap of monolayer Sb from 1.26 eV to 1.0 eV. Elastic constants revealed that Sb nanocrystals possess isotropic mechanical properties. The deformation potential theory calculations showed that mobility can be tuned by changing the layer thickness.

Acknowledgment

SHM gratefully acknowledge the Institute Postdoctoral fellowship (IPDF) from Department of Chemistry at IIT Kanpur. VKY acknowledge the funding from Department of Science and Technology (MHRD F. NO. 5-6/2013 TS-VII). The authors also acknowledge Dr. Thiruvancheril G. Gopakumar for fruitful discussion and the HPC centre IIT Kanpur for providing computational facility.

Appendix A. Supplementary data

Supplementary data to this article can be found online at https://doi.org/10.1016/j.jpcs.2019.109156.

References

[1] S.D. Sarma, S. Adam, E.H. Hwang, Enrico Rossi, Electronic transport in two-dimensional graphene, Rev. Mod. Phys. 83 (2) (2011) 407.
[2] Y. Pan, L. Zhang, L. Huang, L. Li, L. Meng, et al., Construction of 2D atomic crystals on transition metal surfaces: graphene, silicene, and hafnene, Small 10 (11) (2014) 2215–2225.
[3] Y. Zhang, T.T. Tang, C. Girit, Z. Hao, M.C. Martin, A. Zettl, M.F. Crommie, Y.R. Shen, Feng Wang, Direct observation of a widely tunable bandgap in bilayer graphene, Nature 459 (7248) (2009) 820.
[4] Y. Jing, Z. Zhou, C.R. Cabrera, Z. Chen, Graphene, inorganic graphene analogs and their composites for lithium ion batteries, J. Mater. Chem. 2 (31) (2014) 12104–12122.
[5] S. Zhang, Z. Yan, Y. Li, Z. Chen, H. Zeng, Atomically thin arsenene and antimonene: semimetal–semiconductor and indirect–direct band-gap transitions, Angew. Chem. Int. Ed. 54 (10) (2015) 3112–3115.
[6] S. Cahangirov, M. Topsakal, E. Akturk, H. Şahin, S. Ciraci, Two-and one-dimensional honeycomb structures of silicon and germanium, Phys. Rev. Lett. 102 (23) (2009) 236804.
[7] A.J. Mannix, X.F. Zhou, B. Kiraly, J.D. Wood, D. Alducin, B.D. Myers, X. Liu, B.L. Fisher, U. Santiago, J.R. Guest, M.J. Yacaman, Synthesis of borophenes: anisotropic, two-dimensional boron polymorphs, Science 350 (6267) (2015) 1513–1516.
[8] S.H. Mir, S. Chakraborty, P.C. Jha, J. Warna, H. Soni, P.K. Jha, R. Ahuja, Two-dimensional boron: lightest catalyst for hydrogen and oxygen evolution reaction, Appl. Phys. Lett. 109 (5) (2016) 053903.
[9] O. Akturk, V. Uzengi, O. Ozçelik, S. Ciraci, Single-layer crystalline phases of antimony: Antimonenes, Phys. Rev. B 91 (23) (2015) 235446.
[10] Ş. Hasan, S. Cahangirov, M. Topsakal, E. Bekaroglu, E. Akturk, R.T. Senger, S. Ciraci, Monolayer honeycomb structures of group-IV elements and III-V binary compounds: first-principles calculations, Phys. Rev. B 80 (15) (2009) 155453.
[11] M. Daniel, C. Neiss, F. Vines, A. Gorling, Competition for graphene: graphynes with direction-dependent Dirac cones, Phys. Rev. Lett. 108 (8) (2012) 086804.
[12] V.K. Yadav, S.H. Mir, J.K. Singh, Density functional theory study of aspirin adsorption on BCN sheets and their hydrogen evolution reaction activity: a comparative study with graphene and hexagonal boron nitride, ChemPhysChem 20 (2019) 687–694.
[13] S.H. Mir, V.K. Yadav, J.K. Singh, Boron-carbon-Nitride sheet as a novel surface for biological applications: insights from density functional theory, ACS Omega 4 (2019) 3732–3738.
[14] V.K. Yadav, H. Chakraborty, M.L. Klein, U.V. Waghmare, C.N.R. Rao, Defect-enriched tunability of electronic and charge-carrier transport characteristics of 2D Borocarbonitride (BCN) monolayers from ab initio calculations, Nanoscale (2019),

https://doi.org/10.1039/C9NR04096J.
[15] C. Yim, M. O'Brien, N. McEvoy, S. Winters, I. Mirza, J.G. Lunney, G.S. Duesberg, Investigation of the optical properties of MoS_2 thin films using spectroscopic ellipsometry, Appl. Phys. Lett. 104 (10) (2014) 103114.
[16] C. Ataca, S. Ciraci, Functionalization of single-layer MoS2 honeycomb structures, J. Phys. Chem. C 115 (27) (2011) 13303–13311.
[17] S.H. Mir, S. Chakraborty, J. Warna, S. Narayan, P.C. Jha, P.K. Jha, R. Ahuja, A comparative study of hydrogen evolution reaction on pseudo-monolayer WS_2 and PtS_2: insights based on the density functional theory, Catalysis Science & Technology 7 (3) (2017) 687–692.
[18] G. Wang, R. Pandey, S.P. Karna, Atomically thin group V elemental films: theoretical investigations of antimonene allotropes, ACS Appl. Mater. Interfaces 7 (21) (2015) 11490–11496.
[19] C. Kamal, E.M. Arsenene, Two-dimensional buckled and puckered honeycomb arsenic systems, Phys. Rev. B 91 (2015) 085423.
[20] F. Xia, H. Wang, Y. Jia, Rediscovering black phosphorus as an anisotropic layered material for optoelectronics and electronics, Nat. Commun. 5 (2014) 4458.
[21] C.A. Gomez, L. Vicarelli, E. Prada, J.O. Island, K.L. Narasimha-Acharya, S.I. Blanter, D.J. Groenendijk, et al., Isolation and characterization of few-layer black phosphorus, 2D Mater. 1 (2) (2014) 025001.
[22] J.D. Wood, S.A. Wells, D. Jariwala, K.S. Chen, E. Cho, V.K. Sangwan, X. Liu, L.J. Lauhon, T.J. Marks, M.C. Hersam, Effective passivation of exfoliated black phosphorus transistors against ambient degradation, Nano Lett. 14 (12) (2014) 6964–6970.
[23] J. Jianping, X. Song, J. Liu, Z. Yan, C. Huo, S. Zhang, M. Su, et al., Two-dimensional antimonene single crystals grown by van der Waals epitaxy, Nat. Commun. 7 (2016) 13352.
[24] M. Zhao, X. Zhang, L. Li, Strain-driven band inversion and topological aspects in Antimonene, Sci. Rep. 5 (2015) 16108.
[25] J. Lee, W.C. Tian, W.L. Wang, D.X. Yao, Two-dimensional pnictogen honeycomb lattice: structure, on-site spin-orbit coupling and spin polarization, Sci. Rep. 5 (2015) 11512.
[26] T. Lei, C. Liu, J.L. Zhao, J.M. Li, J.O. Wang, R. Wu, H.J. Qian, K. Ibrahim, Y.P. Li, H.Q. Wang, Electronic structure of antimonene grown on Sb_2Te_3(111) and Bi_2Te_3 substrates, J. Appl. Phys. 119 (1) (2016) 015302.
[27] P. Ares, Fernando Aguilar-Galindo, David Rodriguez-San-Miguel, D.A. Aldave, Sergio Diaz-Tendero, M. Alcami, F. Martin, Julio Gomez-Herrero, F. Zamora, Mechanical isolation of highly stable antimonene under ambient conditions, Adv. Mater. 28 (30) (2016) 6332–6336.
[28] H.S. Tsai, C.W. Chen, C.H. Hsiao, H. Ouyang, J.H. Liang, The advent of multilayer antimonene nanoribbons with room temperature orange light emission, Chem. Commun. 52 (54) (2016) 8409–8412.
[29] V.K. Yadav, S.H. Mir, J.K. Singh, A computational study of structural, electronic and carrier mobility of boron and phosphorus/nitrogen co-doped graphene, Phys. B Condens. Matter 571 (2019) 291–295 https://doi.org/10.1016/j.physb.2019.07.017.
[30] S. Bruzzone, G. Fiori, Ab-initio simulations of deformation potentials and electron mobility in chemically modified graphene and two-dimensional hexagonal boron-nitride, Appl. Phys. Lett. 99 (2011) 222108.
[31] P. Giannozzi, S. Baroni, N. Bonini, M. Calandra, R. Car, et al., QUANTUM ESPRESSO: a modular and open-source software project for quantum simulations of materials, J. Phys. Condens. Matter 21 (39) (2009) 395502.
[32] J.P. Perdew, K. Burke, M. Ernzerhof, Phys. Rev. Lett. 77 (18) (1996) 3865.
[33] J.P. Perdew, J.A. Chevary, S.H. Vosko, K.A. Jackson, M.R. Pederson, D.J. Singh, C. Fiolhais, Phys. Rev. B 46 (1992) 6671.
[34] H.J. Monkhorst, J.P. Pack, Special points for Brillouin-zone integrations, Phys. Rev. B 13 (1976) 5188.
[35] S. Grimme, J. Antony, S. Ehrlich, H. Krieg, A consistent and accurate ab initio parametrization of density functional dispersion correction (DFT-D) for the 94 elements H-Pu, J. Chem. Phys. 132 (2010) 154104.
[36] S. Baroni, S.D. Gironcoli, A.D. Corso, P. Giannozzi, Phonons and related crystal properties from density-functional perturbation theory, Rev. Mod. Phys. 73 (2) (2001) 515.
[37] S.H. Mir, P.C. Jha, S. Dabhi, P.K. Jha, Ab initio study of phase stability, lattice dynamics and thermodynamic properties of magnesium chalcogenides, Mater. Chem. Phys. 175 (2016) 54–61.
[38] D.R. Hamann, M. Schlüter, C. Chiang, Norm-conserving pseudopotentials, Phys. Rev. Lett. 43 (20) (1979) 1494.
[39] X. Wang, K. Kunc, I. Loa, U. Schwarz, K. Syassen, Effect of pressure on the Raman modes of antimony, Phys. Rev. B 74 (13) (2006) 134305.
[40] J. Zheng, Y. Wang, L. Wang, R. Quhe, Z. Ni, et al., Interfacial properties of bilayer and trilayer graphene on metal substrates, Sci. Rep. 3 (2013) 2081.
[41] A.C. Ferrari, Raman spectroscopy of graphene and graphite: disorder, electron–phonon coupling, doping and nonadiabatic effects, Solid State Commun. 143 (2007) 47–57.
[42] https://magicplot.com/.
[43] L. Hong, Q. Zhang, C. Chong, R. Yap, B.K. Tay, et al., From bulk to monolayer MoS2: evolution of Raman scattering, Adv. Funct. Mater. 22 (7) (2012) 1385–1390.
[44] C. Lee, H. Yan, L.E. Brus, T.F. Heinz, J. Hone, S. Ryu, Anomalous lattice vibrations of single-and few-layer MoS_2, ACS Nano 4 (5) (2010) 2695–2700.
[45] Y. Wang, P. Huang, M. Ye, R. Quhe, Y. Pan, et al., Many-body effect, carrier mobility, and device performance of hexagonal arsenene and antimonene, Chem. Mater. 29 (5) (2017) 2191–2201.
[46] O.D. Restrepo, K.E. Krymowski, J. Goldberger, W. Windl, A first principles method to simulate electron mobilities in 2D materials, New J. Phys. 16 (2014) 105009.
[47] X. Li, J.T. Mullen, Z. Jin, K.M. Borysenko, M.B. Nardelli, K.W. Kim, Intrinsic electrical transport properties of monolayer silicene and MoS2 from first principles, Phys. Rev. B Condens. Matter Mater. Phys. 87 (2013) 115418.